# Unmasking the Origin of Kinks in the Photoemission Spectra of Cuprate Superconductors

Zhenglu Li, Meng Wu, Yang-Hao Chan, and Steven G. Louie

Phys. Rev. Lett. **126**, 146401 — Published 8 April 2021

DOI: 10.1103/PhysRevLett.126.146401

# Unmasking the Origin of Kinks in the Photoemission Spectra of Cuprate Superconductors

Zhenglu Li, Meng Wu, Yang-Hao Chan, and Steven G. Louie*

*Department of Physics, University of California at Berkeley, Berkeley, CA 94720, USA and Materials Sciences Division, Lawrence Berkeley National Laboratory, Berkeley, CA 94720, USA.*

*Email: sglouie@berkeley.edu

**Abstract**

The origin of a ubiquitous bosonic coupling feature in the photoemission spectra of high-$T_c$ cuprates, an energy-momentum dispersion 'kink' observed at ~70 meV binding energy, remains a two-decade-old mystery. Understanding this phenomenon requires an accurate description of the coupling between the electron and some collective modes. We report here *ab initio* calculations based on *GW* perturbation theory and show that correlation-enhanced electron-phonon interaction in cuprates gives rise to the strong kinks, which not only explains quantitatively the observations but provides new understanding of experiments. Our results reveal it is the electron density-of-states being the predominant factor in determining the doping-dependence of the kink size, manifesting the multi-band nature of the cuprates, as opposed to the prevalent belief of it being a measure of the mode-coupling strength.

**Main text**

Rich exotic phases in copper oxide superconductors (the cuprates) arise from correlated electrons and their interactions with other elementary excitations [1]. Over the past two decades, intensive angle-resolved photoemission spectroscopy (ARPES) experiments have established a major bosonic coupling fingerprint in the cuprates – namely, along the *d*-wave superconducting gap nodal direction in the reciprocal space, the quasiparticle dispersion relation kinks at a binding energy around 70–80 meV [2–4]. A phonon mechanism was initially conjectured [3] because the kink's energy matches that of the oxygen breathing phonon energy [5–9] and later supported by multiple-mode features [10] and the isotope effect [11,12]. On the other hand, spin fluctuations were also proposed as an alternative mechanism [4,13], as well as a boson-free mechanism that had been suggested [14]. The debate on the physical origin of the kink is yet to be settled because there are various collective excitations or bosonic modes in the cuprates, any of which may lead to a similar phenomenon with properly fitted model parameters [9,13,14] to experimental data. To provide unbiased conclusions, predictive first-principles approaches (with no adjustable parameters) become necessary.

Knowing the origin of the photoemission kink would provide new insights to interactions in this important class of materials and may lead to better understanding of other phenomena including superconductivity. A major impediment has been a lack of truly *ab initio* calculations that can quantitatively explain the kink feature. In particular, within the mechanism of electron-phonon (*e*-ph) coupling induced kink, previous calculations [5,6] – based on *ab initio* density-functional theory (DFT) [15,16,17] – yielded a kink that is nearly a factor of 3 too small in magnitude as compared with experiments. Meanwhile, there are yet to be any *ab initio* studies capable of explaining the kink quantitatively in a parameter-free fashion with other proposed mechanisms. It is however important to note that standard static DFT fundamentally does not address the excited states of materials [18,19]; its naive application to the coupling between the excited quasiparticles and other elementary excitations can be severely misrepresented in some materials [17,20]. Thus, even within the *e*-ph mechanism, it remains unclear whether the observed discrepancy is due

to the inadequacy of the standard DFT formulation of the *e*-ph coupling (i.e., treating the electrons as the fictitious Kohn-Sham noninteracting electrons) or indeed phonons are not involved. Here we address this question using a newly developed method – *GW* perturbation theory (*GW*PT) [20] – that has successfully included many-electron correlation effects in computing the *e*-ph interaction from first principles. The *e*-ph coupling is properly computed as the interaction of a true quasiparticle (including nonlocal self-energy effects) with the phonons, within a linear-response and interacting-Green's-function formalism in the *GW* approximation [18–20].

We investigate the *e*-ph interaction and photoemission kinks in the prototypical single-copper-oxygen-layer cuprate $La_{2-x}Sr_xCuO_4$ (LSCO) in the optimally doped ($x = 0.15$) and overdoped ($x = 0.30$) hole concentrations. We do not address the underdoped cuprates in this work because they possess very strong local correlations [1] for which the application of quasiparticle-based *GW*PT formalism may not be properly justified. We find that, correlation effects included in *GW*PT significantly enhances the phonon-induced part of the quasi-electron self-energy by a factor of 2–3 as compared with results from DFT *e*-ph coupling [5,6] as obtained from density functional perturbation theory (DFPT) [16,17]. The calculated kink magnitude, as well as its doping and temperature dependence, quantitatively agree with a broad range of experiments [3,21–26], showing that the nodal photoemission kink in cuprates is mainly caused by *e*-ph coupling. The excellent agreement with experiments from first principles enables us to proceed with confident to dissect the hidden interplays among the *e*-ph interaction, electronic structure, and photoemission kink of the cuprates, which can often be obscured in the experimental data and subjected to speculation. Indeed, from optimally doped to overdoped regime, our results show a reduced kink size in agreement with experiments. However, contrary to the common interpretation [3,4,21–26] attributing this doping dependence of the kink size to a weakening electron-boson coupling strength, our analysis clearly shows that this is in fact due to a multi-band density-of-states (DOS) effect previously not recognized.

An excited electron or hole in a crystal interacts with other electrons and elementary excitations including phonons, acquiring a shift in its excitation energy and a finite lifetime. These many-body interaction effects may be formally cast into a complex operator called the self-energy $\Sigma$ associated with a quasiparticle, and can be measured in ARPES experiments. The *GW* method [18,19,27] expands the electron-electron part of the self-energy to first order in the Green's function ($G$) and in the screened Coulomb interaction ($W$), i.e. $\Sigma^{e-e}(\mathbf{r}, \mathbf{r}'; \varepsilon) = iGW$, capturing the non-local ($\mathbf{r}, \mathbf{r}'$) and frequency ($\varepsilon$) dependence of the interaction. The *e*-ph coupling matrix element describes the amplitude of an electron being coupled from one quasiparticle state to another, due to changes in the potentials (both crystal potential and self-energy) induced by phonons seen by the electron, which can be efficiently evaluated via linear-response theory [16,17,20]. The *GW*PT approach [20] directly computes the changes in the electronic self-energy due to perturbing phonons (with phonon wavevector $\mathbf{q}$ and branch index $\nu$), $\partial_{\mathbf{q}\nu}\Sigma^{e-e}(\mathbf{r}, \mathbf{r}'; \varepsilon)$, in constructing the *e*-ph matrix elements – a core ingredient of microscopic *e*-ph theories including electron correlation effects. (See theoretical and computational details, along with a *GW*PT validation set of five conventional metals and one oxide metal, in the Supplemental Material [28].)

Having accurate *ab initio* *e*-ph interactions allows us to compute the *phonon-induced* part of the electron's self-energy $\Sigma^{e-\mathrm{ph}}$, which reshapes the electron dispersion relation and provides notable phonon-induced signatures if any (such as kinks in ARPES). For comparison, we calculate the *e*-ph properties of LSCO using both *GW*PT- and DFPT-calculated *e*-ph matrix elements, together with a Wannier interpolation technique [59]. Figure 1 shows the nodal $\Sigma^{e-\mathrm{ph}}_{n\mathbf{k}}(E_{n\mathbf{k}})$ (with electron wavevector $\mathbf{k}$ and band index $n$) computed within the Fan-Migdal approximation [17,60–62] at low temperature ($T = 20$ K). In Figs. 1(a) and 1(b), $\mathrm{Re}\Sigma^{e-\mathrm{ph}}_{n\mathbf{k}}$ shows a dominant peak at 75 meV and 76 meV binding energy for $x = 0.15$ and $x = 0.30$, respectively, whose origin is traced to come from the Cu-O in-plane half- and full-breathing modes as found previously [5]. The calculated peak positions nicely agree with the experimentally measured kink positions [3,21] at around 70–80 meV binding energies. The shoulder structure near 40 meV is due to the oxygen buckling and stretching modes [5]. Beyond the maximum phonon frequency $\omega_{\mathrm{ph}}^{\mathrm{max}} = 87$ meV,

$\mathrm{Re}\Sigma_{n\mathbf{k}}^{e-\mathrm{ph}}$ behaves as a featureless flat tail up to 200 meV binding energies without any peaks. Figures 1(c) and 1(d) show a roughly double-step structure in the magnitude of $\mathrm{Im}\Sigma_{n\mathbf{k}}^{e-\mathrm{p}}$ (with step positions corresponding to the abovementioned 40 meV and 75 meV phonon modes) and then slowly decays beyond $\omega_{\mathrm{ph}}^{\mathrm{max}}$ up to 200 meV binding energy [28]. Importantly, for both $x$ = 0.15 and $x$ = 0.30, the peak magnitude of $\mathrm{Re}\Sigma_{n\mathbf{k}}^{e-\mathrm{ph}}$ and $\mathrm{Im}\Sigma_{n\mathbf{k}}^{e-\mathrm{ph}}$ within the phonon frequency range is around 25–35 meV from *GW*PT, but is only 10–15 meV from DFPT, representing a correlation enhancement in the *e*-ph induced self-energy by a factor of about 2–3, which is directly reflected in the kink magnitude as discussed below.

We now explore in detail the low-energy (<100 meV) region in the nodal dispersion relation where phonons produce sharp features, although spectroscopic features exist at higher binding energies [63,64] as well. Experimental extraction of the exact size and position of the kink in the measured quasiparticle dispersion relation depends on the choice of a reference bare band [65]. The common practice is to assume the bare band (i.e., without the effects of bosonic mode coupling of interest) as a straight line that connects the quasi-hole state at Fermi energy $E_F$ (set to zero throughout this paper) to another state at an arbitrarily chosen lower energy $E_1$, which had often taken a range from at –0.1 to –0.3 eV in the literature [3,4,10–12,21–26,63,64,66]. In this practice, the deviation at each **k** point of the measured dispersion relation from the assumed reference line is usually mis-labeled as "Re$\Sigma$", although it is in fact *not* the real part of the self-energy. Here, we shall follow this experimental practice to extract the size and location of the kinks to make direct comparisons between theoretical and experimental data. To emphasize the low-energy bosonic-coupling contributions, we choose $E_1$ = –0.12 eV (similar to many experiments) such that the extracted kink covers all the rapidly varying features of $\mathrm{Re}\Sigma_{n\mathbf{k}}^{e-\mathrm{ph}}$ while staying away from the high-binding-energy features where coupling to other higher-energy collective excitations may play a role [63–65]. We emphasize that the extracted photoemission kink should be distinguished from the true $\mathrm{Re}\Sigma_{n\mathbf{k}}^{e-\mathrm{ph}}$ that are shown in Fig. 1, and these two quantities are related via Eq. (S7) in the Supplemental Material [28].

Figures 2(a) and 2(c) show the calculated electron spectral functions $A_{n\mathbf{k}}(\omega)$, where the quasiparticle self-energy features (the kink and spectral widths) are clearly visible. We plot the momentum distribution curves (MDCs) at regular energy steps [Figs. 2(b) and 2(d)] and fit each to a Lorentzian function to obtain the MDC-derived energy-*vs*.-wavevector dispersion relation and the linewidth. This data processing procedure is well-defined and is widely adopted in analyzing experimental ARPES spectra [67]. After aligning the reference line for *GW*PT, DFPT, and the experimental dispersion relations to eliminate the unknown bare-band information, a direct comparison of the kink features is made between theory and experiment [3] in Figs. 2(e) and 2(f). We find remarkably good agreement between *GW*PT and experiments [3,21] whereas, as found in previous study [5,6], DFPT dramatically underestimates the kink size. Furthermore, the lifetime information embedded in MDC linewidths shows reasonably good agreement between *GW*PT and experiment [22] [Figs. 2(g) and 2(h)], although a sizable uncertainty depending on the exact fitting procedure to experimental data remains [28]. The reason that the *e*-ph interaction from *GW*PT greatly improves the agreement between theory and experiment is because of its enhanced value from inclusion of electron correlation effects [20].

In Fig. 3, we directly compare the extracted kink features with multiple sets of experimental data [3,21,23–26] on LSCO and $Bi_2Sr_2CuO_{6+\delta}$ (Bi2201) (another single-layer cuprate). Quantitative agreement between the experimental kinks and theoretical *GW*PT kinks is clearly seen [Figs. 3(a) and 3(b)], giving a maximum deviation from the reference line of ~20 meV for optimally doped and ~15 meV for overdoped LSCO and Bi2201, mirroring closely those observed in experiments. We further use the area under the kink-amplitude-*vs*.-energy curve [Figs. 3(a) and 3(b)] at different temperatures for a measure of the temperature dependence of the kink strength, where good agreement between *GW*PT and experiments is also found as seen in Figs. 3(c) and 3(d). The kink strength monotonically reduces as the temperature rises. This is because at higher temperature, both phonon absorption and emission processes become more activated, providing increasingly more scattering channels that would broaden the phonon-induced self-

energy peaks (Fig. S1), leading to a reduced apparent kink size. The quantitative agreement on the temperature dependence of the apparent kink strength between results from *GW*PT and various experiments consolidates the phonon mechanism being the explanation for the 70–80 meV nodal kink in the cuprates (at least as the dominant origin – it is possible other mechanisms [9,13,14] may also contribute in some way). At temperatures below superconducting $T_c$ (~30–40 K for LSCO and Bi2201 at optimal doping), the existence of a non-zero superconducting gap shifts the quasiparticle energies and may have an additional effect (not accounted for in this work) on the experimentally measured kink area [Fig. 3(c)] [9].

The experimental observation of a substantial doping dependence in the cuprate kink size had also been puzzling. From the underdoped towards overdoped regime, the measured apparent kink size monotonically decreases [3,21–23], which has commonly been interpreted as a weakening of the mode-coupling strength (for mechanisms with either phonons or spin fluctuations) [3,4,10,13,26,65,66]. Figure 4(a) plots the doping-dependent kink area data, where the *GW*PT trend also nicely agrees with experiments [3,23]. However, we discovered that this doping dependence in the kink size does not represent a doping dependence in the mode-coupling strength. As seen in Fig. 4(b), the magnitudes of the CuO-plane breathing-mode induced major peak in $\mathrm{Re}\Sigma_{n\mathbf{k}}^{e-\mathrm{ph}}$ (around 75 meV binding energy) at $x = 0.15$ and $x = 0.30$, are nearly identical from our *GW*PT calculations. This finding from our first-principles results is in stark contrast to the common interpretation, and invalidates the conclusion that the bosonic mode-coupling strength weakens with increased hole doping in the cuprates, at least for the phonons.

The observed significant doping dependence in the apparent kink size (as extracted with the commonly used procedure discussed above) is traced back to the tail height of the $\mathrm{Re}\Sigma_{n\mathbf{k}}^{e-\mathrm{ph}}$ at binding energies beyond $\omega_{\mathrm{ph}}^{\max}$. Specifically at $E_1$, $\mathrm{Re}\Sigma_{n\mathbf{k}_1}^{e-\mathrm{ph}}(E_1)$ differs dramatically at the two doping levels [5.3 meV for $x = 0.15$ and 12.8 meV for $x = 0.30$, see Fig. 4(b)], resulting in disparate slopes for the reference line drawn from $E_F$ to $E_1$. Note that the kink is defined as the deviation from the reference line; even if the peak values in $\mathrm{Re}\Sigma_{n\mathbf{k}}^{e-\mathrm{ph}}$ at two different doping levels are alike, the different slopes of the reference lines can give different apparent kink sizes. The difference in the tail height $\mathrm{Re}\Sigma_{n\mathbf{k}_1}^{e-\mathrm{ph}}(E_1)$ at different doping levels is largely caused by features in the electron DOS distribution, reflecting the multiband nature of the cuprates. We demonstrate this effect with rigid-band approximation calculations: using the as-calculated electron band structure, phonon dispersions, *e*-ph matrix elements at $x = 0.15$, we recompute $\Sigma_{n\mathbf{k}}^{e-\mathrm{ph}}$ after rigidly shifting $E_F$ to the corresponding value at $x = 0.30$ (to isolate the DOS effects on the kinks). As shown in Fig. 4(b) (and Fig. S2), the shift of $E_F$ to higher hole doping level (without changing the *e*-ph matrix elements) significantly elevates the tail height in $\mathrm{Re}\Sigma_{n\mathbf{k}}^{e-\mathrm{ph}}$. This arises because the non-resonant contributions to $\mathrm{Re}\Sigma_{n\mathbf{k}_1}^{e-\mathrm{ph}}(E_1)$ are inversely correlated to the energy difference between $E_1$ and the final states (denoted as $\Delta E$). The calculated electron band structure and DOS [Figs. 4(c)–(e)] show that at $x = 0.30$, the quasi-hole at $E_1$ has a larger amplitude to be non-resonantly scattered into the deeper final electronic states (smaller $\Delta E$ from $E_1$ to the rise of part of the DOS below –0.2 eV and to further deeper states) than at $x = 0.15$, resulting in a higher value for $\mathrm{Re}\Sigma_{n\mathbf{k}_1}^{e-\mathrm{ph}}(E_1)$, and thus a decreased apparent kink size (see Eq. (S7) in Supplemental Material [28]). We further note that although DFTP calculation also includes this multi-band DOS effect, its unrealistically small *e*-ph coupling values fail to capture the correct doping trend in the kink size [Fig. 4(a)].

In summary, first-principles *GW*PT calculations of LSCO have identified that the correlation-enhanced *e*-ph interaction is the main origin of the ubiquitous 70–80 meV dispersion kink in the ARPES of cuprates, and revealed that the multi-band DOS effect plays a requisite role in understanding the doping dependence of the extracted apparent kink size. The quantitative agreement with experiments indicates that *GW*PT satisfactorily captures the correlation effects in *e*-ph coupling matrix elements in optimally doped and overdoped cuprates, where the quasiparticle picture is still appropriate [68–70].

## References


[1] B. Keimer, S. A. Kivelson, M. R. Norman, S. Uchida, and J. Zaanen, From quantum matter to high-temperature superconductivity in copper oxides, Nature **518**, 179–186 (2015).

[2] T. Valla *et al.*, Evidence for quantum critical behavior in the optimally doped cuprate $Bi_2Sr_2CaCu_2O_{8+\delta}$, Science **285**, 2110–2113 (1999).

[3] A. Lanzara, *et al.*, Evidence for ubiquitous strong electron–phonon coupling in high-temperature superconductors, Nature **412**, 510–514 (2001).

[4] P.-D. Johnson *et al.*, Doping and temperature dependence of the mass enhancement observed in the cuprate $Bi_2Sr_2CaCu_2O_{8+\delta}$, Phys. Rev. Lett. **87**, 177007 (2001).

[5] F. Giustino, M. L. Cohen, and S. G. Louie, Small phonon contribution to the photoemission kink in the copper oxide superconductors, Nature **452**, 975–978 (2008).

[6] R. Heid, K.-P. Bohnen, R. Zeyher, and D. Manske, Momentum dependence of the electron-phonon coupling and self-energy effects in superconducting $YBa_2Cu_3O_7$ within the local density approximation, Phys. Rev. Lett. **100**, 137001 (2008).

[7] D. Reznik, G. Sangiovanni, O. Gunnarsson, and T. P. Devereaux, Photoemission kinks and phonons in cuprates, Nature **455,** E6–E7 (2008).

[8] K.-P. Bohnen, R. Heid, and M. Krauss, Phonon dispersion and electron-phonon interaction for $YBa_2Cu_3O_7$ from first-principles calculations, Europhys. Lett. **64**, 104–110 (2003).

[9] T. P. Devereaux, T. Cuk, Z.-X. Shen, and N. Nagaosa, Anisotropic electron-phonon interaction in the cuprates, Phys. Rev. Lett. **93**, 117004 (2004).

[10] X. J. Zhou *et al.*, Multiple bosonic mode coupling in the electron self-energy of $(La_{2-x}Sr_x)CuO_4$, Phys. Rev. Lett. **95**, 117001 (2005).

[11] G. Gweon *et al.*, An unusual isotope effect in a high-transition-temperature superconductor, Nature **430**, 187–190 (2004).

[12] H. Iwasawa *et al.*, Isotopic fingerprint of electron-phonon coupling in high-$T_c$ cuprates, Phys. Rev. Lett. **101**, 157005 (2008).

[13] T. Dahm *et al.*, Strength of the spin-fluctuation-mediated pairing interaction in a high-temperature superconductor, Nature Phys. **5,** 217–221 (2009).

[14] K. Byczuk *et al.*, Kinks in the dispersion of strongly correlated electrons, Nature Phys. **3**, 168–171 (2007).

[15] R. O. Jones, O. Gunnarsson, The density functional formalism, its applications and prospects, Rev. Mod. Phys. **61**, 689 (1989).

[16] S. Baroni, S. De Gironcoli, A. Dal Corso, and P. Giannozzi, Phonons and related crystal properties from density-functional perturbation theory, Rev. Mod. Phys. **73**, 515 (2001).

[17] F. Giustino, Electron-phonon interactions from first principles, Rev. Mod. Phys. **89**, 015003 (2017).

[18] M. S. Hybertsen and S. G. Louie, First-principles theory of quasiparticles: calculation of band gaps in semiconductors and insulators, Phys. Rev. Lett. **55**, 1418 (1985).

[19] M. S. Hybertsen and S. G. Louie, Electron correlation in semiconductors and insulators: band gaps and quasiparticle energies, Phys. Rev. B **34**, 5390 (1986).

[20] Z. Li, G. Antonius, M. Wu, F. H. da Jornada, and S. G. Louie, Electron-phonon coupling from *ab initio* linear-response theory within the *GW* method: correlation-enhanced interactions and superconductivity in $Ba_{1-x}K_xBiO_3$, Phys. Rev. Lett. **122**, 186402 (2019).

[21] X. J. Zhou *et al.*, Universal nodal Fermi velocity, Nature **423**, 398 (2003).

[22] X. J. Zhou, Z. Hussain, Z.-X. Shen, High resolution angle-resolved photoemission study of high temperature superconductors: charge-ordering, bilayer splitting and electron–phonon coupling, Journal of Electron Spectroscopy and Related Phenomena **126**, 145–162 (2002).

[23] S. R. Park *et al.*, Broken relationship between superconducting pairing interaction and electronic dispersion kinks in $La_{2-x}Sr_xCuO_4$ measured by angle-resolved photoemission, Phys. Rev. B **88**, 220503 (2013).

[24] T. Kondo *et al.*, Anomalous doping variation of the nodal low-energy feature of superconducting $(Bi,Pb)_2(Sr,La)_2CuO_{6+\delta}$ crystals revealed by laser-based angle-resolved photoemission spectroscopy, Phys. Rev. Lett. **110**, 217006 (2013).

[25] W. S. Lee *et al.*, Superconductivity-induced self-energy evolution of the nodal electron of optimally doped $Bi_2Sr_2Ca_{0.92}Y_{0.08}Cu_2O_{8+\delta}$, Phys. Rev. B **77**, 140504 (2008).

[26] Y.-Y. Peng *et al.* Doping evolution of nodal band renormalization in $Bi_2Sr_2CuO_{6+\delta}$ superconductor revealed by laser-based angle-resolved photoemission spectroscopy, Chin. Phys. Lett. **30**, 067402 (2013).

[27] L. Hedin, New Method for Calculating the One-Particle Green's Function with Application to the Electron-Gas Problem, Phys. Rev. **139**, A796 (1965).

[28] See Supplemental Material for computational details, theoretical formalism, extraction of experimental data, more discussions on the *e*-ph behavior in LSCO, and a *GW*PT validation set of five conventional metals (Cu, Al, In, ZrN, and Nb) and one oxide metal, which includes Refs. [29–58].

[29] X. Gonze *et al.*, ABINIT: First-principles approach to material and nanosystem properties, Comput. Phys. Commun. **180**, 2582–2615 (2009).

[30] J. Deslippe *et al.*, BerkeleyGW: A massively parallel computer package for the calculation of the quasiparticle and optical properties of materials and nanostructures, Comput. Phys. Commun. **183**, 1269–1289 (2012).

[31] M. Del Ben, C. Yang, Z. Li, F. H. da Jornada, S. G. Louie, and J. Deslippe, Accelerating Large-Scale Excited-State GW Calculations on Leadership HPC Systems, in *2020 SC20: International Conference for High Performance Computing, Networking, Storage and Analysis (SC), Atlanta, GA, US,* pp36–46 (2020).

[32] S. Poncé, E. R. Margine, C. Verdi, and F. Giustino, EPW: Electron–phonon coupling, transport and superconducting properties using maximally localized Wannier functions, Comput. Phys. Commun. **209**, 116–133 (2016).

[33] D. Hamann, Optimized norm-conserving Vanderbilt pseudopotentials, Phys. Rev. B **88**, 085117 (2013).

[34] M. J. van Setten *et al.*, The PseudoDojo: Training and grading a 85 element optimized norm-conserving pseudopotential table, Comput. Phys. Commun. **226**, 39-54 (2018).

[35] J. P. Perdew, K. Burke, and M. Ernzerhof, Generalized gradient approximation made simple, Phys. Rev. Lett. **77**, 3865 (1996).

[36] I. Souza, N. Marzari, and D. Vanderbilt, Maximally localized Wannier functions for entangled energy bands, Phys. Rev. B **65**, 035109 (2001).

[37] A. A. Mostofi *et al.*, An updated version of wannier90: A tool for obtaining maximally-localised Wannier functions, Comput. Phys. Commun. **185**, 2309–2310 (2014).

[38] O. Hellman, I. A. Abrikosov, and S. I. Simak, Lattice dynamics of anharmonic solids from first principles, Phys. Rev. B **84**, 180301 (2011).

[39] J.-J. Zhou, O. Hellman, and M. Bernardi, Electron-phonon scattering in the presence of soft modes and electron mobility in $SrTiO_3$ perovskite from first principles, Phys. Rev. Lett. **121**, 226603 (2018).

[40] G. Kresse and J. Hafner, *Ab initio* molecular dynamics for liquid metals, Phys, Rev. B **47**, 558 (1993).

[41] G. Kresse and D. Joubert, From ultrasoft pseudopotentials to the projector augmented-wave method, Phys. Rev. B **59**, 1758 (1999).

[42] T. Tadano, Y. Gohda, and S. Tsuneyuki, Anharmonic force constants extracted from first-principles molecular dynamics: applications to heat transfer simulations, J. Phys. Condens. Matter **26**, 225402 (2014).

[43] C. Faber *et al.*, Exploring approximations to the *GW* self-energy ionic gradients, Phys. Rev. B **91**, 155109 (2015).

[44] M. Rohlfing and S. G. Louie, Electron-hole excitations in semiconductors and insulators, Phys. Rev. Lett. **81**, 2312 (1998).

[45] M. Rohlfing and S. G. Louie, Electron-hole excitations and optical spectra from first principles, Phys. Rev. B **62**, 4927 (2000).

[46] G. Onida, L. Reining, and A. Rubio, Electronic excitations: density-functional versus many-body Green's-function approaches, Rev. Mod. Phys. **74**, 601 (2002).

[47] E. L. Wolf, in *Principles of Electronic Tunneling Spectroscopy: Second Edition*, Oxford University Press (2012).

[48] M. J. G. Lee, J. Caro, D. G. de Groot, and R. Griessen, Point-contact spectroscopy of copper, Phys. Rev. B **31**, 8244 (1985).

[49] J. Zasadzinski, D. M. Burnell, E. L. Wolf, and G. B. Arnold, Superconducting tunneling study of vanadium, Phys. Rev. B **25**, 1622 (1982).

[50] E. L. Moore, R. W. Reed, and F. G. Brickwedde, Single-particle electron-tunneling investigation of the phonon spectra and superconductivity of indium-tin alloys, Phys. Rev. B **15**, 187 (1977).

[51] J. Geerk, G. Linker, and R. Smithey, Electron tunneling into superconducting ZrN, Phys. Rev. Lett. **57**, 3284 (1986).

[52] J. Bostock, M. L. A. MacVicar, G. B. Arnold, J. Zasadzinski, and E. L.Wolf, The Current Status Of Experimental Tunneling Results On Niobium, *in Superconductivity in d- and f-Band Metals*, Pages 153-158 (1980).

[53] Q. Huang, J. F. Zasadzinski, N. Tralshawala, K. E. Gray, D. G. Hinks, J. L. Peng, and R. L. Greene, Tunnelling evidence for predominantly electron–phonon coupling in superconducting $Ba_{1-x}K_xBiO_3$ and $Nd_{2-x}Ce_xCuO_{4-y}$, Nature **347**, 369 (1990).

[54] S. Y. Savrasov and D. Y. Savrasov, Electron-phonon interactions and related physical properties of metals from linear-response theory, Phys. Rev. B **54**, 16487 (1996).

[55] R. Bauer, A. Schmid, P. Pavone, and D. Strauch, Electron-phonon coupling in the metallic elements Al, Au, Na, and Nb: A first-principles study, Phys. Rev. B **57**, 11276 (1998).

[56] S. P. Rudin, R. Bauer, A. Y. Liu, and J. K. Freericks, Reevaluating electron-phonon coupling strengths: Indium as a test case for *ab initio* and many-body theory methods, Phys. Rev. B **58**, 14511 (1998).

[57] R. Heid, K.-P. Bohnen, B. Renker, T. Wolf, and H. Schober, *Ab initio* lattice dynamics and electron-phonon coupling in the refractory compounds ZrN and HfN, Phys. Rev. B **71**, 092302 (2005).

[58] J. Bostock, V. Diadiuk, W. N. Cheung, K. H. Lo, R. M. Rose, and M. L. A. Mac Vicar, Does Strong-Coupling Theory Describe Superconducting Nb?, Phys. Rev. Lett. **36**, 603 (1976).

[59] F. Giustino, M. L. Cohen, and S. G. Louie, Electron-phonon interaction using Wannier functions, Phys. Rev. B **76**, 165108 (2007).

[60] A. B. Migdal, Interaction Between electrons and lattice vibrations in a normal metal, Soviet Physics JETP, 7, 996–1001 (1958).

[61] P. B. Allen and B. Mitrović, Theory of superconducting $T_c$, Solid State Phys. **37**, 1–92 (1983).

[62] G. Grimvall, The Electron-Phonon Interaction in Metals, *in Series of Monographs on Selected Topics in Solid State Physics* **16** (1981).

[63] T. Valla *et al.*, High-energy kink observed in the electron dispersion of high-temperature cuprate superconductors, Phys. Rev. Lett. **98**, 167003 (2007).

[64] W. Meevasana *et al.*, Hierarchy of multiple many-body interaction scales in high-temperature superconductors, Phys. Rev. B **75**, 174506, (2007).

[65] W. Meevasana *et al.*, Doping dependence of the coupling of electrons to bosonic modes in the single-layer high-temperature $Bi_2Sr_2CuO_6$ superconductor, Phys. Rev. Lett. **96**, 157003 (2006).

[66] I. M. Vishik *et al*., Doping-dependent nodal Fermi velocity of the high-temperature superconductor $Bi_2Sr_2CaCu_2O_{8+\delta}$ revealed using high-resolution angle-resolved photoemission spectroscopy, Phys. Rev. Lett. **104**, 207002 (2010).

[67] A. Damascelli, Z. Hussain, and Z.-X. Shen, Angle-resolved photoemission studies of the cuprate superconductors, Rev. Mod. Phys. **75**, 473 (2003).

[68] Y. He *et al.* Rapid change of superconductivity and electron-phonon coupling through critical doping in Bi-2212, Science **362**, 62–65 (2018).

[69] J. Chang *et al.*, Anisotropic quasiparticle scattering rates in slightly underdoped to optimally doped high-temperature $La_{2-x}Sr_xCuO_4$ superconductors, Phys. Rev. B **78**, 205103 (2008).

[70] J. Chang *et al.*, Anisotropic breakdown of Fermi liquid quasiparticle excitations in overdoped $La_{2-x}Sr_xCuO_4$, Nature Commun. **4**, 2559 (2013).

**Acknowledgments**

This work was supported by the Theory of Materials Program at the Lawrence Berkeley National Laboratory (LBNL) through the Office of Basic Energy Sciences, U.S. Department of Energy under Contract No. DE-AC02-05CH11231, which provided for the DFPT and *GW*PT calculations, and by the National Science Foundation under Grant No. DMR-1926004, which provided for the Wannier interpolation calculations and relevant analysis. Advanced codes were provided by the Center for Computational Study of Excited-State Phenomena in Energy Materials (C2SEPEM) at LBNL, which is funded by the U.S. Department of Energy, Office of Science, Basic Energy Sciences, Materials Sciences and Engineering Division under Contract No. DE-AC02-05CH11231, as part of the Computational Materials Sciences Program. An award of computer time was provided by the Innovative and Novel Computational Impact on Theory and Experiment (INCITE) program. Significant amount of computational resources were needed in this work, and were provided by the following computing centers: Stampede2 at the Texas Advanced Computing Center (TACC) through Extreme Science and Engineering Discovery Environment (XSEDE), which is supported by National Science Foundation under Grant No. ACI-1053575; Summit at the Oak Ridge Leadership Computing Facility through the INCITE program, which is a DOE Office of Science User Facility supported under Contract No. DE-AC05-00OR22725; Cori at National Energy Research Scientific Computing Center (NERSC), which is supported by the Office of Science of the U.S. Department of Energy under Contract No. DE-AC02-05CH11231; Frontera at TACC, which is supported by National Science Foundation under Grant No. OAC-1818253. Z.L. acknowledges Y. He for many fruitful discussions and for sharing experimental perspectives. The authors thank A. Lanzara, G. Antonius, F. da Jornada, M. Del Ben, C. Yang, J. Deslippe, T. Cao, Z.-X. Li, M. Yi, C. S. Ong, H. J. Choi, and S. Ju for helpful discussions.

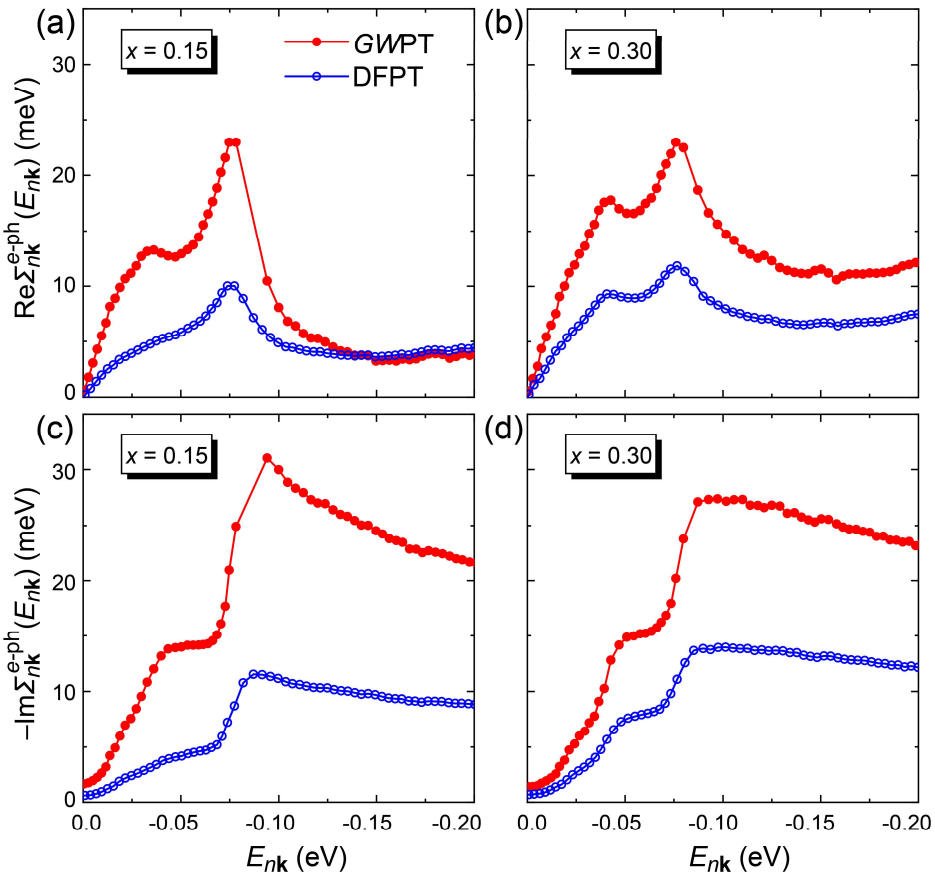


FIG. 1. (a),(b) Contribution of electron-phonon coupling to the real part of the nodal electron self-energy $\mathrm{Re}\Sigma_{n\mathbf{k}}^{e-\mathrm{ph}}$ for (a) optimally doped ($x$ = 0.15) and (b) overdoped ($x$ = 0.30) LSCO at $T$ = 20 K, calculated using $e$-ph matrix elements from $GW$PT (red solid dots) and DFPT (blue empty dots). The Fermi energy $E_F$ is set to zero. (c),(d) Imaginary part of the phonon-induced contribution ($T$ = 20 K) to the electron self-energy $\mathrm{Im}\Sigma_{n\mathbf{k}}^{e-\mathrm{ph}}$, the magnitude of which continuously rises until the maximum phonon frequency $\omega_{\mathrm{ph}}^{\mathrm{max}}$ ~ 87 meV.

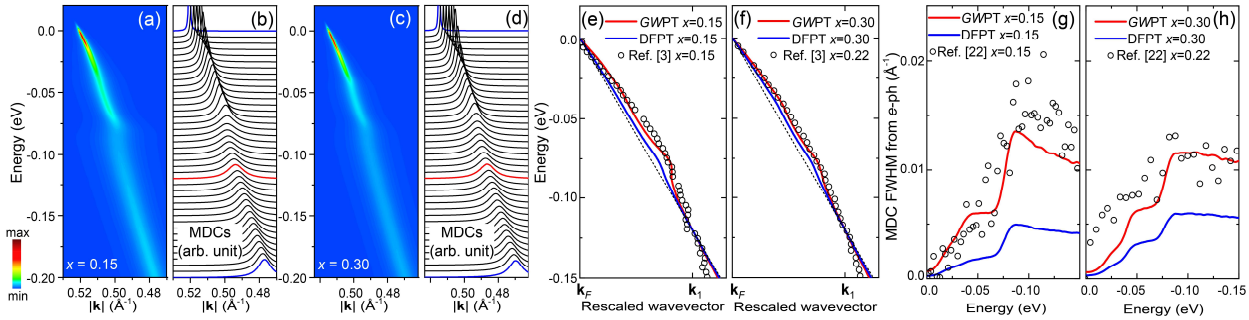


FIG. 2. (a) Spectral function $A_{n\mathbf{k}}(\omega)$ (plotted in color scale) calculated with $\Sigma_{n\mathbf{k}}^{e-\mathrm{ph}}(\omega)$ using *GW*PT for optimally doped ($x$ = 0.15) LSCO at $T$ = 20 K, along the nodal direction in the Brillouin zone. (b) Momentum-distribution curves (MDCs) at each energy slice between $E_F$ and –0.2 eV with 0.005 eV spacing. Each MDC is fitted to a Lorentzian function to get the peak position and linewidth. The MDCs at the extremal energies are indicated by the blue lines. The red line is the MDC at $E_1$ = –0.12 eV whose peak position is used to determine the bare-band straight reference line (connecting the peaks at $E_F$ and $E_1$ on a given dispersion relation). (e) Comparison of MDC-derived dispersion relation between experiment (open circles) [3] and theory from *GW*PT (red line) and DFPT (blue line), after aligning the reference line (black dashed line). $\mathbf{k}_F$ is the Fermi wavevector and $\mathbf{k}_1$ is the wavevector corresponding to $E_1$. (g) The *e*-ph contribution to the full-width-at-half-maximum (FWHM) of MDC peaks extracted from experiments (open circles) [22] and from *GW*PT (red line) and DFPT (blue line). (c),(d),(f),(h) Similar to (a),(b),(e),(g) but for overdoped LSCO.

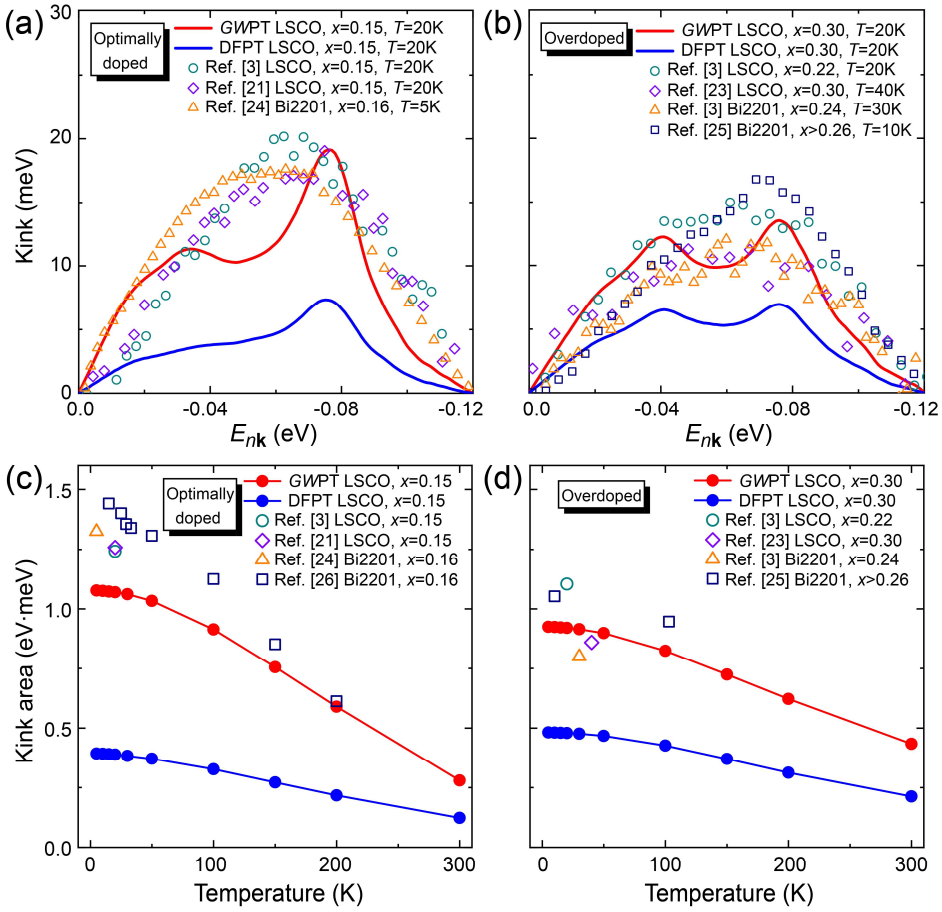


FIG. 3. (a),(b) Kink size as a function of quasiparticle-state energy, extracted as the deviation of the MDC-derived dispersion relation from the straight reference line (see Fig. 2). Data shown are from various experiments [3,21,23–26] on LSCO and Bi2201 (open symbols) and from the calculations of LSCO using *GW*PT (red dots) and DFPT (blue dots), at the optimally doped and overdoped regimes. (c),(d) Total kink area, defined as the area under the curve in (a) and (b), as a function of temperature.

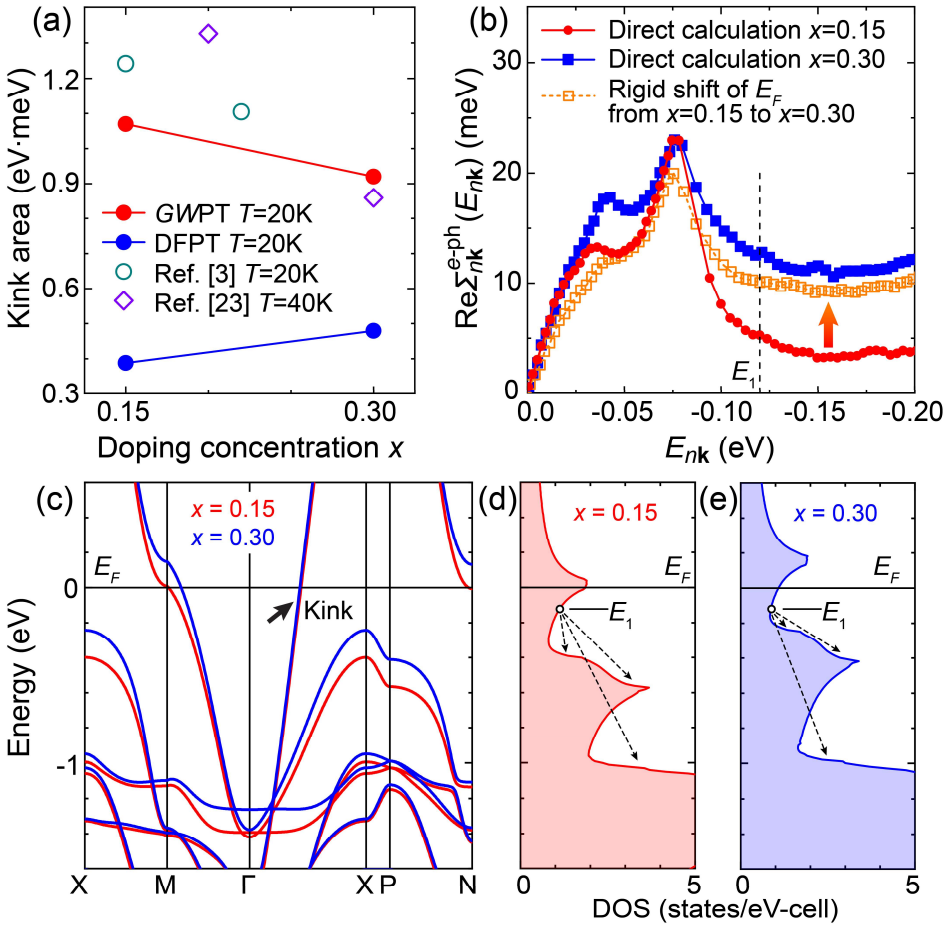


FIG. 4. (a) Doping dependence in the total apparent kink area of LSCO from experiments [3,23], *GW*PT, and DFPT calculations. (b) Direct calculations of $\mathrm{Re}\Sigma_{n\mathbf{k}}^{e-\mathrm{ph}}$ at $x$ = 0.15 (red solid dot) and $x$ = 0.30 (blue solid squares) at $T$ = 20 K. The orange empty squares represent a rigid-band approximation calculation with a rigid shift of $E_F$ from that of $x$ = 0.15 to that of $x$ = 0.30 in constructing $\Sigma_{n\mathbf{k}}^{e-\mathrm{ph}}$ (i.e. the band structure, phonon dispersions, and $e$-ph matrix elements remain unchanged at the $x$ = 0.15 level), resulting in the elevation of the self-energy tail, as indicated by the arrow. (c) Band structure of LSCO at $x$ = 0.15 and $x$ = 0.30. The black arrow points to the position of the kink along the Γ–X nodal direction. (d),(e) DOS of LSCO at the indicated two doping levels. The scatterings (indicated by arrow-headed dashed lines) of quasi-hole from $E_1$ to higher-binding-energy hole final states with significant DOS have larger energy separations (thus contributing less to $\mathrm{Re}\Sigma_{n\mathbf{k}_1}^{e-\mathrm{ph}}(E_1)$) at $x$ = 0.15 than at $x$ = 0.30.